33RD CONGRESS
OF THE INTERNATIONAL COUNCIL
OF THE AERONAUTICAL SCIENCES
STOCKHOLM, SWEDEN, 4–9 SEPTEMBER, 2022

ICAS 2022 SWEDEN

NUMERICAL AND EXPERIMENTAL STRUCTURAL CHARACTERIZATION OF COMPOSITE ADVANCED JOINT FOR ULTRA LIGHT AEROSPACE PLATFORMS

Polla A.[1,2], Frulla G.[1], Cestino E.[1], Das R.[2] & Marzocca P.[2]

[1]Department of Mechanical and Aerospace Engineering (DIMEAS), Politecnico di Torino, Torino, Italy
[2]Department of Aerospace Engineering and Aviation, School of Engineering, RMIT University, Melbourne, Australia

Abstract

In the present work, the results of a numerical campaign aimed to evaluate the progressive damage failure analysis (PDFA) of a specific advanced pin-hole connection under tensile and compressive loads are presented. The proposed numerical models are based on the application of constitutive material models available in LS-DYNA. High fidelity shell-cohesive method was employed to represent composite delamination behavior. In this model each lamina has been modeled separately with the application of interlaminar cohesive elements. Preliminary experimental/numerical correlation indicates that the selected modeling technique predicts experimental results when compared to the proposed laboratory test results. A reduced computational cost has been also determined. The location and extension of the predicted fracture during the damage process are comparable to experimental observations. The proposed methodology demonstrates its preliminary ability to be used for design of composite joints up to failure. Specific outcomes have been also pointed out.

Keywords: Fracture Mechanics, Delamination, Cohesive Elements, LS-DYNA

1. Introduction

Advanced composite materials have been extensively used in recent innovative ultra-light aircraft structures and new reusable launch vehicles for their excellent high strength-to-weight ratio. The combination of solar power and regenerative fuel cell for long endurance ultra-light platforms makes composite materials the best candidates for applications where the configuration and shape depend on the solar/fuel cell efficiency and weight. Due to the dimensions of long-endurance light vehicles, a modular design is requested for manufacturing limits and transportability reasons [1-3]. Removable connections succeed if mechanical bolted joints are used, but, in the case of composite structures (CFRP), the joint has to be properly designed to reach the maximum bearing failure level. The main requirements of the removable platform connection concern: (a) the transmitting of loads between different primary structural parts of the wing spar with a sufficient safety level according to the normative, (b) the guaranteeing of fast assembly and dismounting without any permanent effects on the materials, (c) the positioning of the connected structural parts with the correct clearance. The stress distribution around holes in anisotropic plates under certain load combinations has already been understood [4-5]. However, damage in a composite joint can initiate at an early stage and accumulate inside the laminate as the load increases due to different failure modes. These modes depend to a great extent on the choice of material, ply stacking sequence, laminate thickness, joint geometry, edge effects, bearing, clamping effect, and the loading conditions [6–8]. In general, the validation and verification of the structural composite joints are carried out using a combination of experimental tests and linear static numerical analysis. Nevertheless, the evaluation of failure and post-failure modes is frequently excluded from numerical studies. The lack of fully validated and standardized numerical tools has led to increased use of experimental testing to evaluate the composite structure response according to normative [9]. Therefore, with the increasing use of composite materials, a need for reliable analytical and numerical tools that accurately predict the physical response, damage and failure mechanisms has been established [10-12]. The present work

is based on experimental activities performed by Frulla *et al*. [1] at *Politecnico di Torino* under the "HELINET" project devoted to Solar Powered HALE-UAV design. The proposed joint configuration is a pin-hole connection based on a solid or sandwich CFRP laminate with the same lay-up. The presented laminates have been tested in two different configurations. The former without external steel reinforcement around the fastener hole, the latter with innovative steel reinforcement *Figure 1*. Both configurations have been tested under quasi-static tensile and dynamic loading conditions for applications specific for long endurance ultra-light platforms.

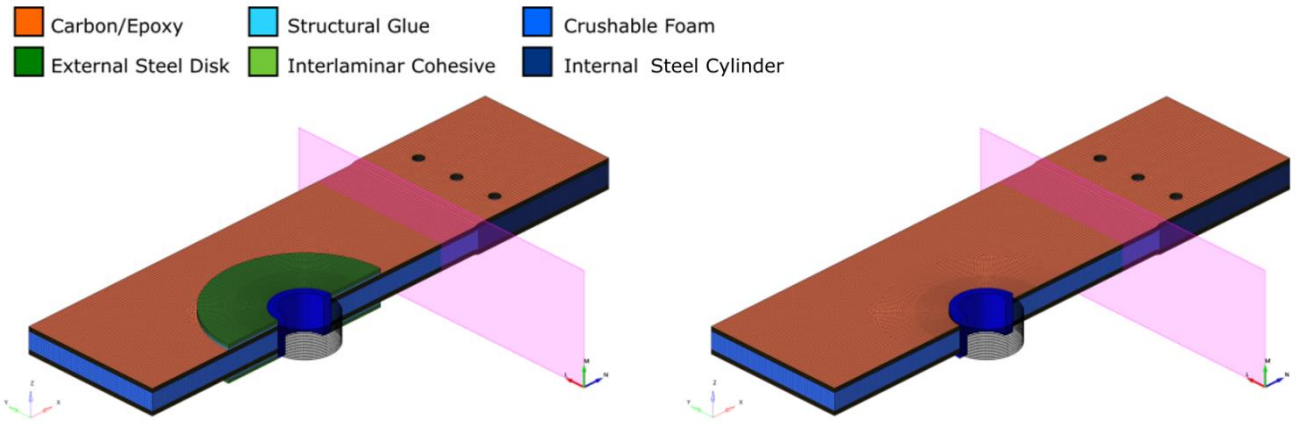

Figure 1: Section of proposed composite joint.

High fidelity shell-cohesive progressive damage failure analysis (PDFA) methods have been proposed to numerically reconstruct the performances of specified samples under tensile and compression loading conditions and thus reduce the design phase of selected structural joints. Complete Stacked Shell modelization technique proposed and described by Polla *et al*. [13] with the application of different material models available in LS-DYNA software package is here proposed. Delamination modeling is investigated with the application of cohesive solid elements capable to reproduce the fracture process observed in damaged composite samples under different critical loads. This paper investigates and evaluates preliminary observations made on selected LS-DYNA composite material models which are capable to capture the fracture response of the aforementioned fastened joint configuration. The presented results are validated against simple experimental data to support modeling features such as modes of failure and physical observed deformations. A subsequent extension to general and complex geometrical composite configurations will be analyzed in future works.

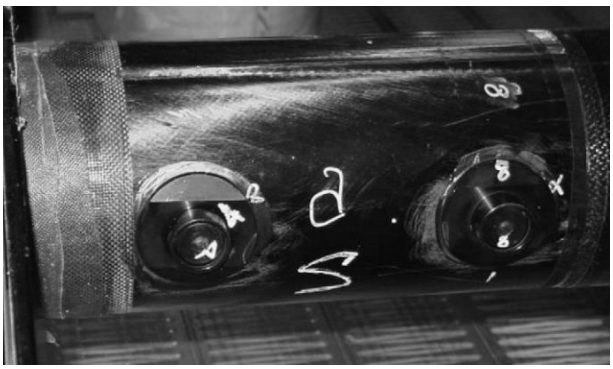

Figure 2: Prototype connection detail [1].

2. Advanced Joint Definition

The presented composite joint configuration was adopted for the installation in the main tubular spar of the *Prototype* structural connection *Figure 2*. The picture shows the proposed configuration with a couple of joints positioned along the midline of the cylindrical tubular spar. Flat samples had been considered for a quick and easy execution of experimental tests even though those real joints were

positioned on a cylindrical surface. All the proposed samples tested in the experimental work were manufactured with the same lay-up and the same Uni-Directional (UD) M40J/epoxy composite material. A sandwich joint was proposed with a 9mm core-thickness of standard Rohacell 51 rigid foam reinforced with glass micro-spheres. Araldite adhesive was used to bond the steel flat plates to the external composite surfaces of the specimens. The reference material vector is directed transversal to the longitudinal axis of the sample (*Figure 3*). The orientation relative to the material axis of the composite joint for a single laminate was chosen in order to obtain the maximum bearing strength $[+20/-20/90/45/-45/90/45/-45]_s$. The nominal thickness of a single laminate panel is 2.16mm and the thickness of a single lamina is around 0.135mm. The material properties are reported in Table [1-3]. The specimens were 240-mm-long, 130-mm-wide with an active zone of damage around the hole of 170-mm-long and 130-mm-wide. The advanced composite joint configuration is reinforced with two external steel plates with an external diameter of 80mm and a thickness of 1.5 mm. The internal steel cylindrical support has an internal diameter of 20mm and a thickness of 3.95 mm for all the advanced joint configurations proposed. The internal cylinder provides the loading transmission between the joint structure and bolt during tensile and compression tests. The sample dimensions are reported in *Figure 3* with the relative position of the Strain-Gauge (SG) applied in experimental tests performed by Frulla *et al*. [1].

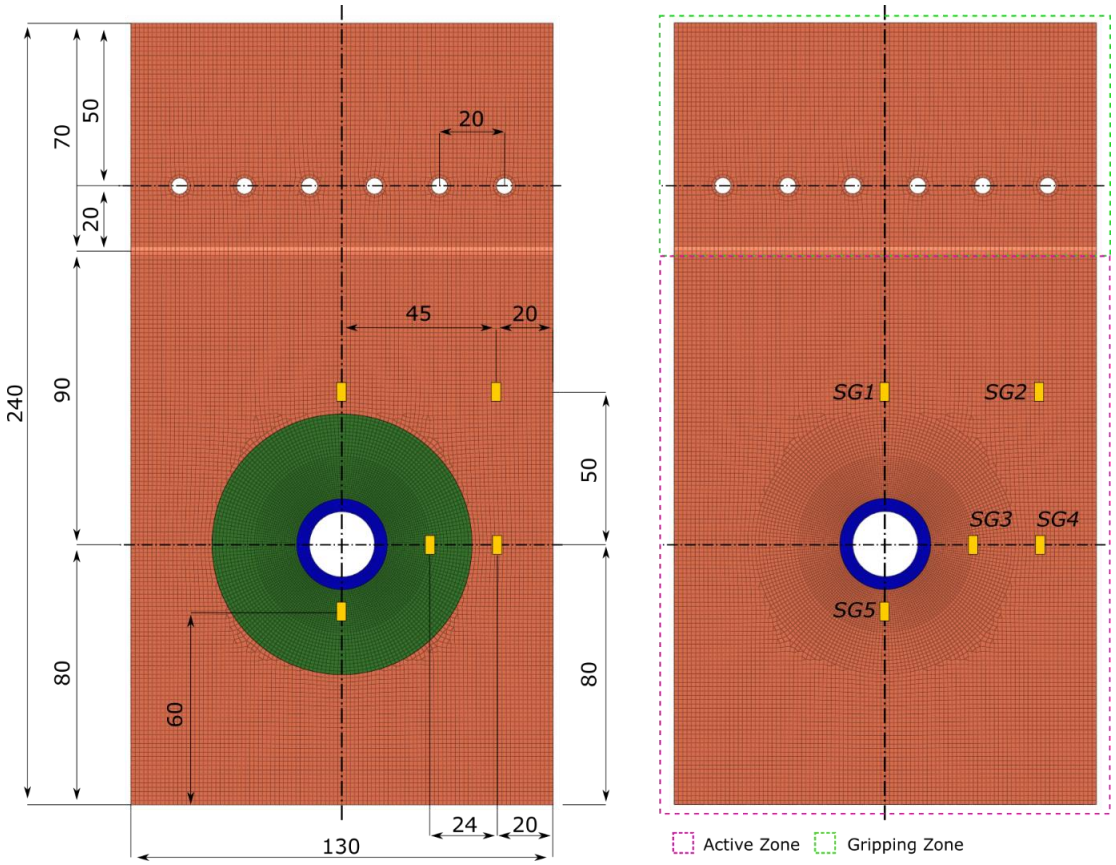

Figure 3: Sample dimension and SG position [mm].

Static and fatigue properties for the proposed flat configuration of the composite joint were obtained from the experimental campaign. The test activity was focused on the solid and sandwich configuration of the composite joint. Experimental activity was performed to understand the modes of failure and the improvement obtained with the application of a bonded steel flat circle plate around the hole. The load was applied up to failure conditions and detailed comparisons were made. The static results are summarized in Table 4. The results obtained show a reduced capacity of the simple solid and sandwich configuration to overcome the typical 20kN pin load even though the joint has been correctly designed to avoid net-tension/shear-out failures and to maximize the bearing strength with a specific lay-up. The average failure load for the solid composite joint was about 20481 N. Sandwich composite joint failure was about 39481 N. On the other hand, the advanced configuration

average failure load was about 94267 N for the solid sample and 97363 N for the sandwich structure. Since no other tests were performed for the prototype application, the results obtained have been used for reference purposes for the correlation with the numerical model proposed in the following sections. The primary objective of this work is to characterize and reproduce the mechanical behavior of the sandwich flat samples with the adoption of explicit LS-DYNA R11.1 solver [20]. The present article is focused on the calibration and validation of the sandwich composite joint FEA explicit model. The proposed models will be used in future work to reproduce and study the mechanics and failure behavior of cylindrical composite joints installed on ultra-light aerospace structures.

Property		*Symbol*	*LS-DYNA parameters*	*Experimental value*
Density	*[kg/mm³]*	ρ	RHO	1.6E-06
Modulus *1-direction*	*[GPa]*	E_1	EA	215.0
Modulus 2-direction	*[GPa]*	E_2	EB	66.7
Shear modulus 12-direction	*[GPa]*	G_{12}	GAB	4.303
Shear modulus 23-direction	*[GPa]*	G_{23}	GBC	3.6
Shear modulus 31-direction	*[GPa]*	G_{31}	GCA	3.6
Major Poisson's ratio	*[-]*	ν_{12}	–	0.27
Minor Poisson's ratio	*[-]*	ν_{21}	$PRBA$	0.0837
Strength 1-direction tension	*[GPa]*	σ_{11}^T	XT	2.365
Strength 2-direction tension	*[GPa]*	σ_{22}^T	YT	0.072
Strength 1-direction tension	*[GPa]*	σ_{11}^C	XC	1.27
Strength 2-direction tension	*[GPa]*	σ_{22}^C	YC	0.14
Shear strength 12-direction	*[GPa]*	τ_{12}	SC	0.063

Table 1: Material properties of M40J/epoxy as published in Frulla et al. [1]

Property		*Symbol*	*LS-DYNA parameters*	*Experimental value*
Density	*[kg/mm³]*	ρ	RHO	5.2E-08
Elastic modulus	*[GPa]*	E_1	E	0.0686
Major Poisson's ratio	*[-]*	ν_{12}	PR	0.05
Yield Stress tension	*[GPa]*	σ_Y	$TSC - SIGP1$	0.00186

Table 2: Material properties of Rohacell 51.

Property		*Symbol*	*LS-DYNA parameter*	*Experimental value*
Density	*[kg/mm²]*	ρ	RHO	8.0E-07
Elastic modulus	*[GPa]*	E_1	E_N	1.7
Shear modulus	*[GPa]*	G_{12}	E_T	0.8
Energy release rate I	*[GPa*mm]*	GIC	GIC	1.10E-03
Energy release rate II	*[GPa*mm]*	$GIIC$	$GIIC$	1.45E-03
Tensile Strength	*[GPa]*	σ^T	T	0.041

Table 3: Material properties of Araldite adhesive.

3. Numerical Modelling Methodology of Composite Advanced Joint

Different numerical techniques are used to accurately reproduce the orthotropic nature of reinforced fiber composite materials depending on which are the details that are necessary to implement in the numerical representation to reconstruct the physical behavior [14-17]. Most of the applications are based on the modelization of the *ply-by-ply* composite structure with the adoption of solid Hexa FEA elements. Kona *et al* [18] modeled composite-fastener joint with one solid element through-thickness for each single lamina. The proposed model was based on the application of the calibrated PDFA

LS-DYNA material model MAT162 extracted from the preceding phase of the NASA ACC HEDI project [9,10]. Moreover, Girolamo *et al.* [19] proposed the same FEA modelization technique to predict the strength of a composite bonded joint under tensile loads. The applicability of *ply-by-ply* FEA solid methods is restricted to small samples and requires high computational resources.

Sample	*Not reinforced [N]*	*Reinforced [N]*
Solid sample - 01	21327	93862
Solid sample - 02	21401	93646
Solid sample - 03	18714	95294
Sandwich sample - 01	39326	97971
Sandwich sample – 02	37500	98924
Sandwich sample - 03	41618	98193

Table 4: Static test results obtained from Frulla et al. [1]

The primary interest of this study is to validate and verify the applicability of the *Complete Stacked Shell* modelization technique (L2DE-Cohesive) proposed and described by Polla *et al*. [13] for the evaluation of complex sandwich structures subjected to tensile and compressive loads. The proposed technique is briefly described in the following subsections and presented in *Figure 4*. For completeness, the description of ply-by-ply solid modeling technique (L2DE-Cohesive) is firstly described, and structured comparisons could be made between the two proposed numerical methodology.

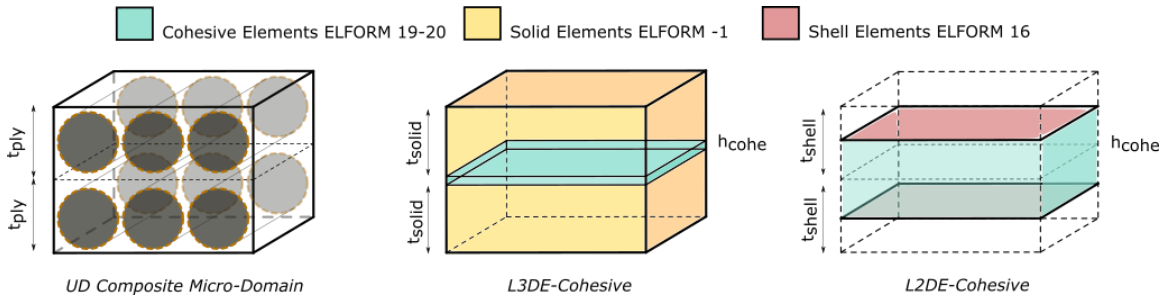

Figure 4: Schematic representation of different FEM-Cohesive models. [13]

3.1 L3DE-Cohesive: 3D Solid with interlaminar cohesive elements

Each composite ply is represented with a layer of solid 3D FEA elements. A single ply is connected to the adjacent one with the introduction of a cohesive interlaminar element with zero thickness (h_{cohe} = *0mm*). LS-DYNA defines for this application a specific element formulation (ELFORM 19) for cohesive elements connected to solid 3D mesh. This modeling practice finds wide application in the industrial and research environment allowing the observation and investigation of the local behavior and off-axis stress-strain relation of the structural component. The major drawback of this method is its complexity and the computational resources necessary to complete the numerical explicit analysis.

3.2 L2DE-Cohesive: 2D Shell with interlaminar cohesive elements

Single plane of 2D shell elements is introduced for each ply belonging to the laminate. Two-dimensional elements plane of a single ply is placed at the geometric mid-surface of each layer. Structural continuity through-thickness is re-established with the application of interlaminar interface elements (cohesive) properly connected to the adjacent ply and commonly inserted with the node-to-node connection. The introduction of cohesive elements restores structural integrity and allows the definition of transverse stiffness and toughness of the composite laminate. ELFORM 20 solid cohesive formulation is introduced for the application with two-dimensional mesh. Compared to the previous case, the cohesive elements will have a non-zero thickness ($h_{cohe} > 0mm$) as described in *Figure 4*.

3.3 Modeling test case

A meso-level approach has been proposed to numerically reconstruct the performances of specified samples under several loading conditions and thus reduce the design phase of selected structural joints. Each carbon/epoxy ply that constitutes the composite laminates was modeled separately with a structured shell surface. L2DE-Cohesive modelization technique was implemented to reproduce the mechanical behavior of specified composite parts. Solid metallic components, core crushable foam, and composite gripping section have been represented with solid Hexa FEM elements. In addition, Araldite adhesive layers were represented with the adoption of solid or cohesive elements. The interlaminar connection between adjacent stacked composite shell layers has been established through the thickness with the application of described solid cohesive elements (ELFORM 20). *PART_COMPOSITE keywords were chosen to define each shell-ply that constitutes composite laminates. A fully-integrated formulation (ELFORM 16) was selected to avoid energy dissipation from hourglass modes. Three Gaussian integration points were defined through the thickness for each composite layer to correctly reproduce bending modes of a single-ply. An efficient fully integrated solid formulation (ELFORM -1) was selected for all solid components. The same formulation (ELFORM -1) was selected for solid adhesives and also a cohesive solid-compatible formulation was applied for the Cohesive Zone Modeling (CZM) structural adhesive section (ELFORM 19). A structured mesh was introduced to improve the quality index of finite elements and improve the energy conservation during the high-deformation fracture process observed in the experimental tests. Consequently, a specific circular and structured mesh alignment was applied around the hole to ensure symmetry and balance condition without stress concentration. A characteristic mesh length parameter was set between 0.35-1.4mm (*Figure 5*).

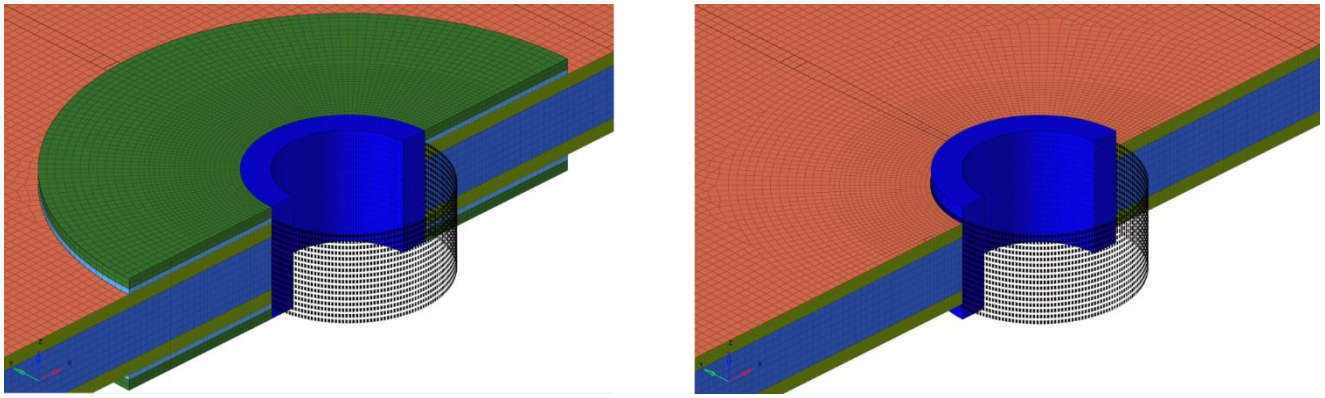

Figure 5: Structured mesh details

Each lamina of the composite laminates was modeled separately and LS-DYNA *CONTACT_SINGLE_SURFACE algorithm was employed to define ply-to-ply post-failure interaction and to reproduce the Coulomb friction that exists between delaminated ply interfaces. Both static and dynamic composite coefficients of friction were set equally to 0.2 and a viscous damping coefficient was introduced equally to 0.05. A contact surface algorithm was introduced to reproduce the load exchanged in the hole between the cylindrical steel support and the sandwich structure during the control displacement loading. An automatic LS-DYNA contact algorithm was introduced (*CONTACT_AUTOMATIC_NODE_TO_SURFACE) to model this interaction. Classic coefficient of friction were set equal to 0.16 for static and 0.11 for the dynamic range. Viscous damping coefficient was introduced for this contact equal to 0.05 to control the damp energy inside the numerical model. Soft constraint formulation (SOFT 1) was set for both contact algorithms. Contact parts are represented in the *Figure 6* with the characteristic distinction between *master* & *slave* groups. Moreover, *CONTACT_INTERIOR algorithm was inserted to avoid negative volume of crushable solid foam when subjected to compression loads. Single point constraints (SPC) were applied to the six-aligned bolts in the gripping area. Constrained xyz-displacements were set to all the through-thickness FEM nodes that constitute the aligned bolts in Gripping Zone *Figure 3*. Prescribed displacement was applied to the rigid cylindrical internal steel hole support to generate

the requested tension load. Progressive Damage Failure Analysis (PDFA) methodology was evaluated with the application of MAT54, MAT58, and MAT59 composite material models. Foam core material is described with the adoption of elastic MAT1 and MAT63 crushable foam models. Adhesive behavior is correctly reproduced with both elastic MAT1 and classic CZM bi-linear curve proposed with MAT138. The pure interlaminar matrix region is modeled with the application of bi-linear cohesive MAT138. A structured comparison is reported between different composite, cohesive and foam material formulations in sequent sections. The simulations were run on LS-DYNA R11.1 explicit single-precision MPP solver. One node on HPC architecture with Intel Xeon Gold 6130 16 cores was adopted. Sandwich FE models with metallic circular flat support have 873318 nodes, 832596 solid elements, and 661632 shell elements. On the other hand, sandwich model without support metallic plate has 836454 node, 795732 solid elements, and 661632 shell elements. Every simulation was completed in a mean of ten hours.

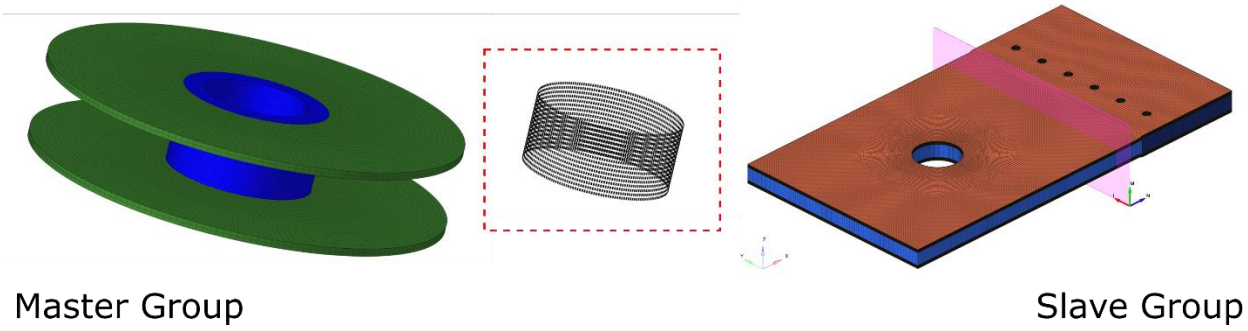

Figure 6: Contact slave & master group.

4. Material model for Progressive Damage Failure Analysis of composite structure

Composite structures have the potential to exhibit different and simultaneous failure mechanisms when subjected to different loading conditions. Tensile and compressive fiber fracture can be observed in combination with intralaminar matrix fracture within CFRP plies. Mixed-mode delaminations can spread between adjacent plies, adhesive layers can deboned from their adherends, and sandwich core can crush under selected loading conditions. All these failure mechanisms interact themselves and influence the final failure mode of the evaluated composite sample. Different progressive damage modeling methodologies are proposed in the literature to account for each of these potential failure mechanisms and their possible interactions. Intralaminar behavior is reproduced with the application of selected composite material models available in LS-DYNA. Interlaminar and adhesive damage modes are represented with the application of cohesive elements and their representative material models. Finally, foam core crushing modes are usually modeled using crushable material models related to closed-cell foam with the correct definition of the characteristic foam curve. No strain-dependent material properties have been evaluated.

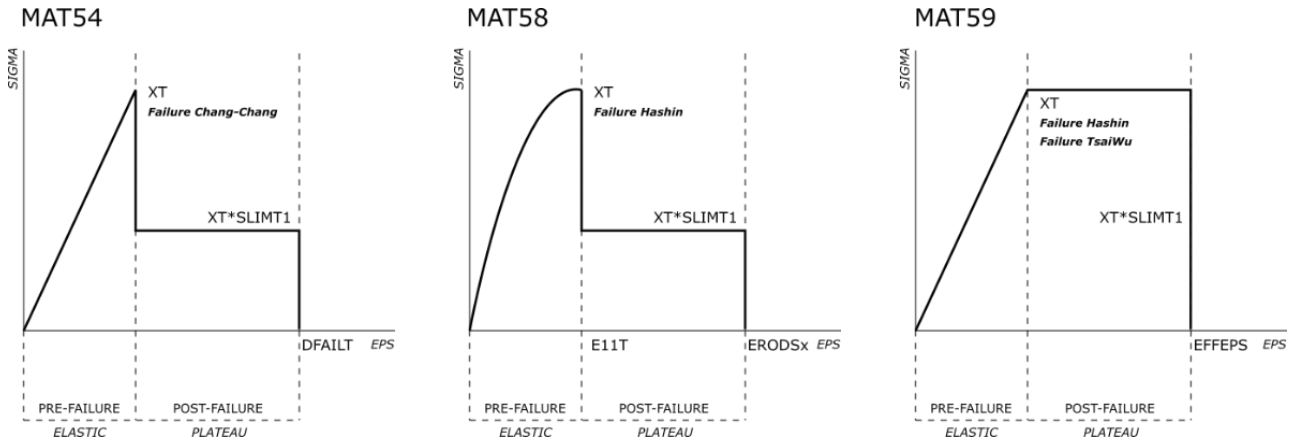

Figure 7: LS-DYNA material model representation.

4.1 Composite material models

Multiple material models are available and different methodologies can be selected. Composite material formulations MAT54, MAT58, and MAT59 are commonly used for carbon/epoxy structures [20]. *MAT_COMPOSITE_DAMAGE (MAT54) imposes an elastoplastic stress-strain relationship with the application of Chang-Chang failure criteria. Maximum strain values (DFAILx) can be defined for reduced orthotropic material direction to control post-failure behaviour and erosion of shell & solid composite FE elements. *MAT_LAMINATED_COMPOSITE_FABRIC (MAT58) is a continuum damage model proposed by Matzenmiller et al [21]. MAT58 defines a smooth stress-strain relation and implements classic Hashin failure criteria to control the damage limit inside a specific element. Post-failure softening values can be defined to describe the residual strength of selected material directions (SLIMxx). Effective strain parameter (ERODS) is used to control the erosion of FEA elements inside the numerical model. *MAT_COMPOSITE_FAILURE_SHELL_MODEL (MAT59) is a faceted or ellipsoidal failure surface material model which does not present any erosion parameter for the shell and solid elements. Specific LS-DYNA *MAT_ADD_EROSION keyword is necessary to control the erosion of the FEA elements and to set the effective strain parameter (EFFEPS) to control the behavior of the presented MAT59 material model. Schematic representation of different material models is reported in *Figure 7*. All material and numerical parameters obtained through a calibration process and adopted for each of the LS-DYNA material formulations are proposed in Table 5-8.

Variable	*Definition*	*Inserted value*
SLIMT1	Post failure maximum stress limit 1-tension	0.25
SLIMT2	Post failure maximum stress limit 2-tension	0.9
SLIMC1	Post failure maximum stress limit 1-compression	0.45
SLIMC2	Post failure maximum stress limit 2-compression	0.9
SLIMS	Post failure maximum stress shear direction	0.9

Table 5: MAT54 - MAT58 post failure common input parameter.

Variable MAT54	*Definition*	*Inserted value*
DFAILM	Max strain for matrix straining in tension and compression	0.30
DFAILS	Max shear strain	0.15
TFAIL	Time step criteria for element deletion	1.0e-08
SOFT	Crush front strength reducing parameter	1.0
FBRT	Softening factor for fiber tensile	1.0
YCFAC	Softening factor for fiber compressive	9.07
DFAILT	Max strain for fiber tension	0.4
DFAILC	Max strain for fiber compression	-0.12
EFS	Effective failure strain	0.0

Table 6: MAT54 numerical input parameter.

Variable MAT58	*Definition*	*Inserted value*
TFAIL	Time step criteria for element deletion	1.0e-08
ERODS	Maximum effective strain for element failure	-0.3
E11C	Strain at longitudinal compressive strength	0.0065
E11T	Strain at longitudinal tensile strength	0.0012
E22C	Strain at transverse compressive strength	0.00231
E22T	Strain at transverse tensile strength	0.0012
GMS	Engineering shear strain at shear strength	0.03144

Table 7: MAT58 numerical input parameter.

Variable MAT59	*Definition*	*Inserted value*
TFAIL	Time step criteria for element deletion	1.0e-08
SOFT	Crush front strength reducing parameter	1.0
FBRT	Softening factor for fiber tensile	1.0
SR	SR reduction factor	9.07
SF	SF reduction factor	0.00231
EFFEPS	*MAT_ADD_EROSION Maximum effective strain parameter for element failure	0.0012

Table 8: MAT59 numerical input parameter.

4.2 Cohesive Zone Modeling

Cohesive Zone Modeling (CZM) is a mathematical technique that tries to represent the stress-displacement relation that exist around an initiated material crack. CZM methods are based on a nonlinear numerical procedure reproducing the initiation and evolution of crack and delaminations in a known a priori propagation path. A characteristic bi-linear cohesive curve is described in terms of local stress versus crack opening displacement *Figure 8*. The first segment of the CZM law defines the elastic undamaged region. Specific cohesive stiffness keeps the crack surfaces closed. Different definitions for cohesive stiffness are proposed by Turon et al. [22] for solid-models and by Polla et al. [13] for shell-like structures. CZM elements used to model composite delamination with solid FE elements are usually set to have zero thickness. Very high non-physical artificial cohesive stiffness is necessary to reduce the compliance of the numerical model. Turon et al. (4.2.1) proposed a specific formulation to control the compliance of the entire composite structure. On the other hand, the node-to-node modelization technique implemented with a shell-like structure impose that cohesive element should have a characteristic non-zero thickness. Polla et al. (4.2.2) proposed a formulation to obtain the requested stiffness that satisfies the structure compliance and numerical stability of the model. The second descending segment of the cohesive curve defines the damage evolution of the CZM element. This damage-zone is characteristic for selected cohesive matrix material and for adherent materials adjacent to the cohesive zone. Few authors [19,22] have described the shape of the damage zone for modes I & II and its relevance for the correct numerical representation of physical experimental observations. Several parameters can modify the shape and the evolution of the cohesive fracture zone of the selected thermoplastic and thermoset matrix and for these reasons, further investigation will be necessary to correctly characterize and understand the delamination behavior under selected loading conditions.

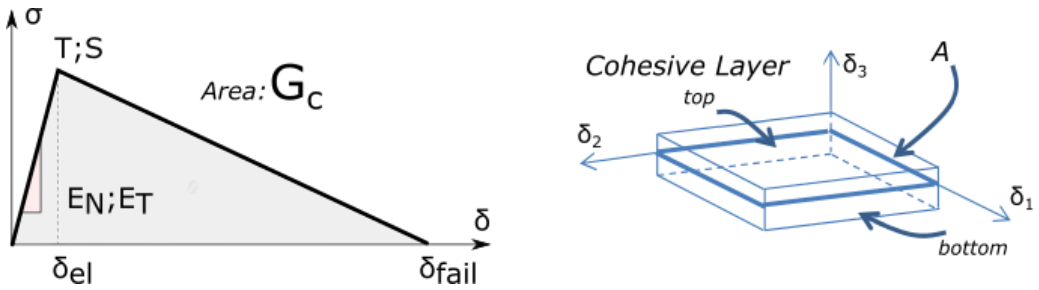

Figure 8: Cohesive constitutive law - bilinear shape; Schematic cohesive element representation with the definition of constitutive displacement relative to the top & bottom surface of adjacent shell layers.

Fracture damage initiates inside a cohesive zone only upon satisfaction of characteristic failure strength. After failure initiation, the stiffness properties of damaged elements soften with further deformation. The area underneath the CZM constitutive law defines the energy necessary to propagate the fracture which is commonly associated with the fracture toughness (G_C). Complete failure displacement is related to the combination of mode I & II strengths and fracture toughness values. *MAT_COHESIVE_MIXED_MODE (MAT138) was selected for the definition of the CZM elements in the interlaminar region between composite plies. ELFORM 20 formulation was chosen due to the L2DE-Cohesive modelization technique selected for this investigation. Cohesive material properties and cohesive stiffness values obtained with the formulations proposed by Polla *et al* [13]

for different parts are reported in Table 9-11. The same material model was applied to model adhesive layers of Araldite between metallic plates and composite surfaces. In contrast, ELFORM 19 was chosen due to the connection to solid mesh of the circular steel plate. Finally, an elastic material model (MAT1) was also applied to make a comparison with the cohesive formulation results obtained for the Araldite adhesive in different numerical models.

$$E_N = \frac{\alpha E_3}{t}; \qquad E_T = \frac{\alpha G_{13}}{t} \qquad \alpha = 25 \div 50 \tag{4.2. 1}$$

$$E_N = \frac{E_3}{t_k + t_{k+1}} = \frac{E_3}{2t_{ply}}; \qquad E_T = \frac{G_{13}}{t_k + t_{k+1}} = \frac{G_{13}}{2t_{ply}} \tag{4.2. 2}$$

Variable MAT138	*Definition*	*Inserted value*
Rho *[kg/mm²]*	Mass per unit volume	8e-07
ROFLG	Density per unit of volume or area	1.0
INTFAIL	N° Integration point for deletion of element	1.0
EN *[GPa/mm]*	Normal cohesive stiffness	28.2
ET *[GPa/mm]*	Tangential cohesive stiffness	16.0
GIC *[GPa*mm]*	Energy release rate for mode I	3.52E-04
GIIC *[GPa*mm]*	Energy release rate for mode II	1.45E-03
XMU	Exponential of the mixed mode criteria	-1.0
T *[GPa]*	Peak traction in normal direction	0.05
S *[GPa]*	Peak traction in tangential direction	0.092

Table 9: MAT138 material parameters for interlaminar region.

Variable MAT138	*Definition*	*Inserted value*
Rho *[kg/mm²]*	Mass per unit volume	8e-07
ROFLG	Density per unit of volume or area	1.0
INTFAIL	N° Integration point for deletion of element	1.0
EN *[GPa/mm]*	Normal cohesive stiffness	315.0
ET *[GPa/mm]*	Tangential cohesive stiffness	120.0
GIC *[GPa*mm]*	Energy release rate for mode I	1.10E-03
GIIC *[GPa*mm]*	Energy release rate for mode II	1.45E-03
XMU	Exponential of the mixed mode criteria	-1.0
T *[GPa]*	Peak traction in normal direction	0.041
S *[GPa]*	Peak traction in tangential direction	0.041

Table 10: MAT138 material parameters for Araldite adhesive.

Variable MAT1	*Definition*	*Inserted value*
Rho *[kg/mm²]*	Mass per unit volume	8e-07
E *[GPa/mm]*	Young modulus	1.7
PR	Poisson ratio	0.3
EFFEPS	*MAT_ADD_EROSION Maximum effective strain parameter for element failure	0.045
VOLEPS	*MAT_ADD_EROSION Volumetric strain at failure	-0.5
NUMFIP	Percentual number of failed integration points	-100

Table 11: MAT1 material properties for Araldite adhesive.

4.3 Core Crush Model

Crushable closed-cell foam core shows fragile behavior in tension and non-linear evolution in compression. Stress-strain relation of crushable foam in compression can be divided into three main regions *Figure 9*: (a) the initial linear-elastic response characterized by Young's modulus of selected foam up to the yield stress; (b) the crushing of the core during which the material has a near-horizontal tangent stiffness; (c) the densification region in which the material start to increase the

stress until its reach the failure stress. *MAT_CRUSHABLE_FOAM (MAT63) was selected to numerically reconstruct the physical behavior of closed-cell foam inserted in sandwich samples. MAT63 is dedicated to modeling crushable foam with optional damping and tension cutoff. The material model requests the definition of the yield stress curve relative to the volumetric strain of the selected foam to reconstruct the non-linear behavior under compression loading (*Figure 9*).
Rohacell 51 stress-strain curve based on material quantities was realized with a specific MATLAB code and inserted in the numerical model. *MAT_ADD_EROSION card was inserted to define tensile stress failure and erosion control parameters for the solid foam elements. In addition, the core crush damage model selected is capable of represent the unloading/reloading response of either a partially or fully crushed material. Finally, an elastic material model (MAT1) was included to make a comparison against the crushable material results obtained for the closed-cell foam. Material values and numerical parameters adopted for these formulations are reported in Table 12-13.

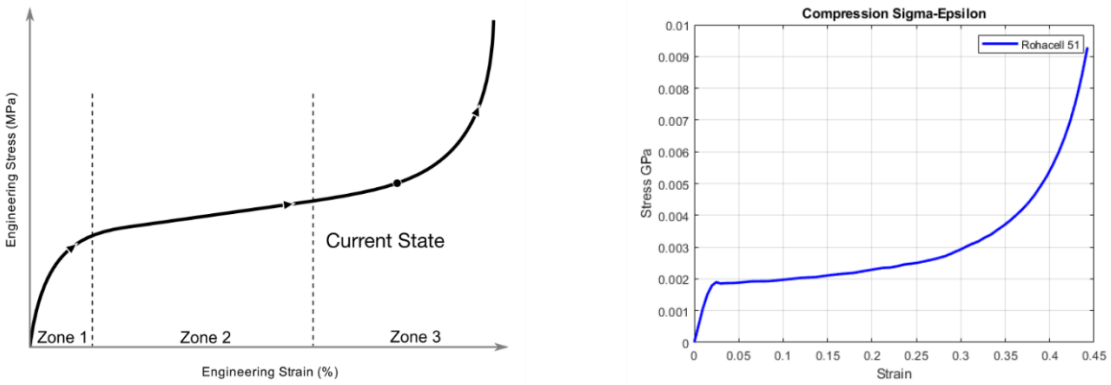

Figure 9: Foam characteristic compression curve; Rohacell 51 foam curve implemented.

Variable MAT63	*Definition*	*Inserted value*
Rho *[kg/mm²]*	Mass per unit volume	5.2e-08
E *[GPa/mm]*	Young modulus	0.0686
PR	Poisson ratio	0.05
TSC *[GPa]*	Tensile stress cutoff	0.00186
EFFEPS	*MAT_ADD_EROSION Maximum effective strain parameter for element failure	0.5
VOLEPS	*MAT_ADD_EROSION Volumetric strain at failure	-0.5
NUMFIP	*MAT_ADD_EROSION Percentual number of failed integration points	-100
SIGP1	* MAT_ADD_EROSION Principal stress at failure	0.00186

Table 12: MAT63 material properties for crushable closed-cell foam.

Variable MAT1	*Definition*	*Inserted value*
Rho *[kg/mm²]*	Mass per unit volume	5.2e-08
E *[GPa/mm]*	Young modulus	0.0686
PR	Poisson ratio	0.05
EFFEPS	*MAT_ADD_EROSION Maximum effective strain parameter for element failure	0.5
VOLEPS	*MAT_ADD_EROSION Volumetric strain at failure	-0.5
NUMFIP	*MAT_ADD_EROSION Percentual number of failed integration points	-100
SIGP1	* MAT_ADD_EROSION Principal stress at failure	0.00186

Table 13: MAT1 material properties for crushable closed-cell foam.

5. Numerical and Experimental Results

Mechanical tension tests were performed in LS-DYNA to evaluate the behavior of composite joints in different configuration for ultra-light aerospace structures. The predicted peak loads of the composite specimen are listed in Table 15-16. The numerical results obtained are compared to the

experimentally observed strength of 97.3 kN and 39.5 kN for both available sandwich configurations. Composite material models proposed in this work (MAT54, MAT58, MAT59) have been evaluated with the combination of two representative close-cell foam material formulation (MAT1 and MAT63). Moreover, the same procedure has been followed to characterize the mechanical performances of Araldite adhesive with the application of elastic and cohesive material model (MAT1, MAT138). A structured comparison has been performed to study and identify the performances of different composite material models available in LS-DYNA R11.1. A total of 24 simulations have been solved on 16 core MPP cluster. Best representation and average results obtained from the numerical simulations are proposed. Table 14 reports nomenclature for the different combinations of material formulations proposed and evaluated for this specific preliminary evaluation.

LS-DYNA Model	Composite *MAT Model*	Foam (Elastic and Damageable) *MAT Model*	Adhesive *MAT Model*
MAT54_MAT1	MAT54	MAT1	MAT1 & MAT138
MAT54_MAT63	MAT54	MAT63	MAT1 & MAT138
MAT58_MAT1	MAT58	MAT1	MAT1 & MAT138
MAT58_MAT63	MAT58	MAT63	MAT1 & MAT138
MAT59_MAT1_HASHIN	MAT59	MAT1	MAT1 & MAT138
MAT59_MAT63_TSAI	MAT59	MAT63	MAT1 & MAT138

Table 14: Nomenclature of proposed numerical models.

Source	*Reinforced [kN]*		
Experimental Sandwich Sample	97.3		
LS-DYNA Model	*First Peak [kN]*	*Second Peak [kN]*	*ERR [%] (Max Peak)*
MAT54_MAT1	87.2	91.9	5.5
MAT54_MAT63	87.2	91.3	6.1
MAT58_MAT1	95.8	99.7	1.5
MAT58_MAT63	96.3	98.5	1.1
MAT59_MAT1_HASHIN	60.8	–	37.5
MAT59_MAT1_TSAI	68.1	–	30.1
MAT59_MAT63_HASHIN	60.7	–	37.6
MAT59_MAT63_TSAI	64.1	–	34.1

Table 15: Reinforced maximum load comparison.

Source	*Not Reinforced [kN]*		
Experimental Sandwich Sample	39.5		
LS-DYNA Model	*First Peak [kN]*	*Second Peak [kN]*	*ERR [%]*
MAT58_MAT1	49.9	–	26.3
MAT58_MAT63	47.3	–	19.7

Table 16: Not reinforced maximum load comparison.

The characteristic force-displacement curve of the advanced composite joint is reported in *Figure 10*. The graph reports two different colored groups of curves obtained by the simulation with the application of MAT58 composite material formulation. Details about the simulation performed are reported in the legend of *Figure 10*. Adopted nomenclature is described in Table 14. Different curves are reported to describe the differences observed with the combination of proposed material models for core structure and adhesive layers. The blue curves group represents the tensile load evolution of the entire sandwich composite joint. The curve can be divided into three characteristic zones: (a) the first elastic part that describes the non-linear evolution of the loading inside the composite structural joint; (b) the second part of the curve that represents the initiation of the failure; (c) the third part that shows the fracture evolution process. The curve is characterized by two distinguished peaks in the failure zone. The first peak represents the initiation of failure inside the composite joint instead the second strength limit defines the failure of the entire sample and the beginning of the global fracture

process. On the other hand, the second group of red curves describes the contact load exchanged between the internal hole steel cylinder and the internal sandwich surface. The peak load of the internal contact force is lower than the failure load of the entire sample. The load difference between the global failure point and the maximum internal contact force is equally distributed around the hole by the presence of the steel circular plate.

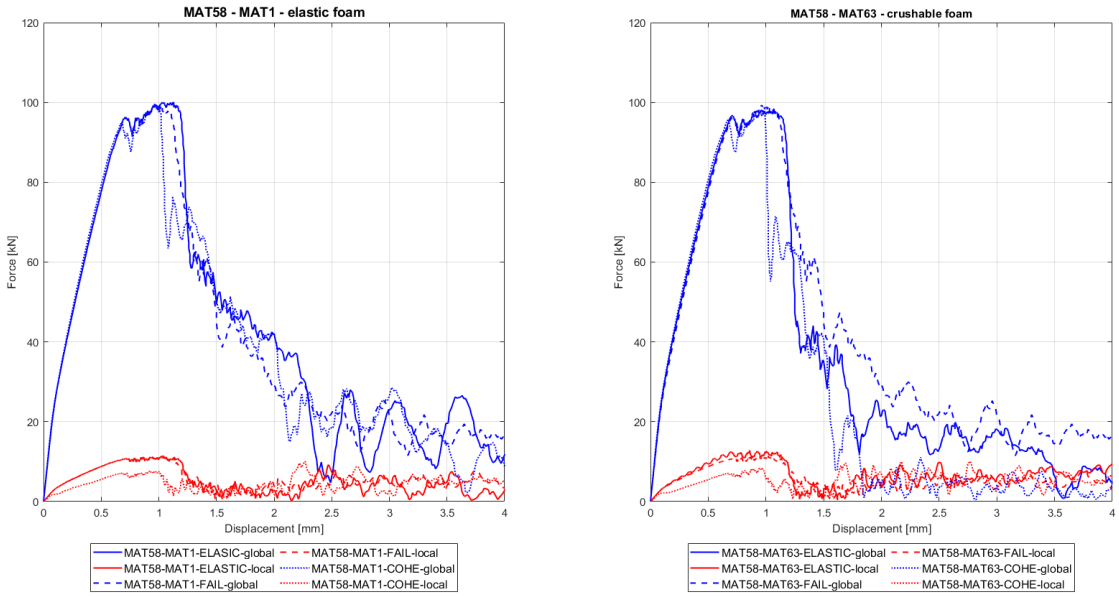

Figure 10: Characteristic force-displacement curve for advanced composite joint. SX: MAT58 composite material model with MAT1 elastic foam. DX: MAT58 composite material model with MAT63 crushable foam.

Proposed MAT54 and MAT58 material models show a good correlation with the experimental results. The complete fracture mode of MAT54 and MAT58 L2DE-Cohesive models is reported in *Figures 11-12*. The fracture surfaces reported for different material combinations show that the principal failure mode for the advanced composite joint is tensile load. Moreover, the images presented demonstrate a relevant incidence to the global failure aspect and to the fracture angle after the modification of foam or adhesive material models.

The average peak loads obtained demonstrate that *MAT_COMPOSITE_DAMAGE and *MAT_LAMINATED_COMPOSITE_FABRIC material models can reproduce the failure mechanisms and strength limit observed experimentally. Relative errors for both numerical models are approximately under 5%. On the other hand, MAT59 shows a reduced capacity to reproduce the failure surfaces and to predict the strength limits. MAT54 and MAT58 are based on a specific material formulation that can be used to describe the elastic and post-failure behavior of composite materials. Instead, MAT59 does not present any parameters to describe and characterize the post-failure behaviour and the plasticity plateau. Both failure criteria implemented in MAT59 fail to describe the evolution of damage inside the proposed composite joint configuration object of this study. *Figure 13* presents the predicted deformation of the advanced composite joint with the implementation of MAT59 for both available failure criteria. Localized damage near the gripping zone and an incorrect softening behaviour is observed in MAT59 results. Different failure mode has been observed experimentally for proposed joint configurations. The principal failure mode for the simple composite joint configuration when subjected to tensile load is under localized compression damage of external laminate panels. The absence of the flat steel circular plate increases the localization of damages around the hole. The calibrated MAT58 material model was implemented to verify the mechanical performances of the simple composite joint. The strength limits observed and reported in Table 16 show that the calibrated numerical parameters implemented in MAT58 for the erosion of the FEA elements (ERODS) are probably incorrect when applied to the simple composite joint. The erosion parameter characteristic of MAT58 was principally calibrated for tensile load deformation and failure in the advanced composite joint configuration. Compressive failure mode for the simple joint configuration requires a specific calibration of the principal numerical parameters available in the proposed LS-DYNA material models. The adoption of the same erosion parameters for a different configuration of tested composite joints

is not possible. The presence of a single erosion parameter in most of the material models limits their applicability to a single loading field. Mixed failure modes require specific and characteristic calibration of the present available erosion parameters.

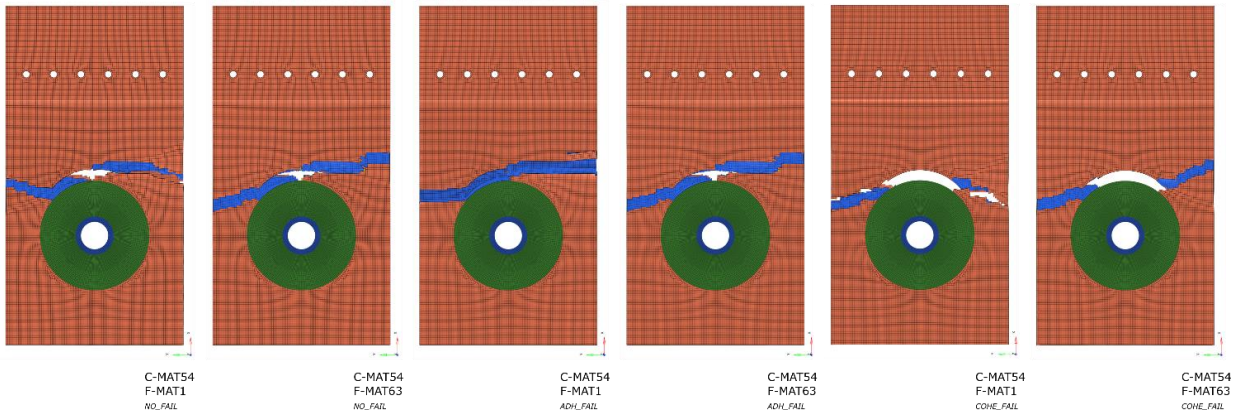

Figure 11: Fracture surface of MAT54 advanced composite joint model.

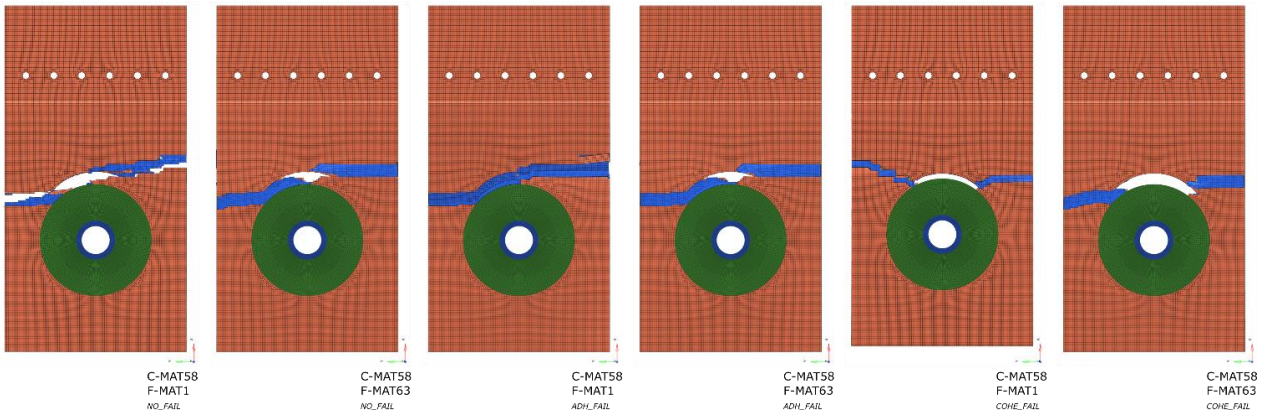

Figure 12: Fracture surface of MAT58 advanced composite joint model.

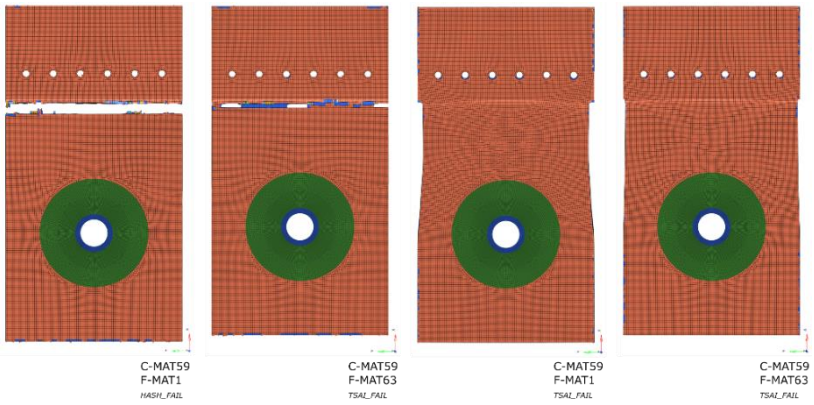

Figure 13: Fracture surface of MAT59 advanced composite joint model.

Figures 14-15 report localized strain value obtained for proposed simple and advanced composite joint configuration at 20 kN of longitudinal tensile load. The punctual strain values obtained in LS-DYNA R11.1 have been compared with the results proposed by Frulla et al. [1]. The position of the selected strain-gauge (SG) is reported in *Figure 3*. The deformation path is in good agreement with literature results for SG 3-4 and SG 5. The strain field differences between the advanced and simple composite joints have been founded also for numerical SG 1-2. Reduced differences have been found in comparison to literature results. A qualitative view of the longitudinal strain distribution has been proposed. Extended evaluation of stress-strain will be proposed in future work.

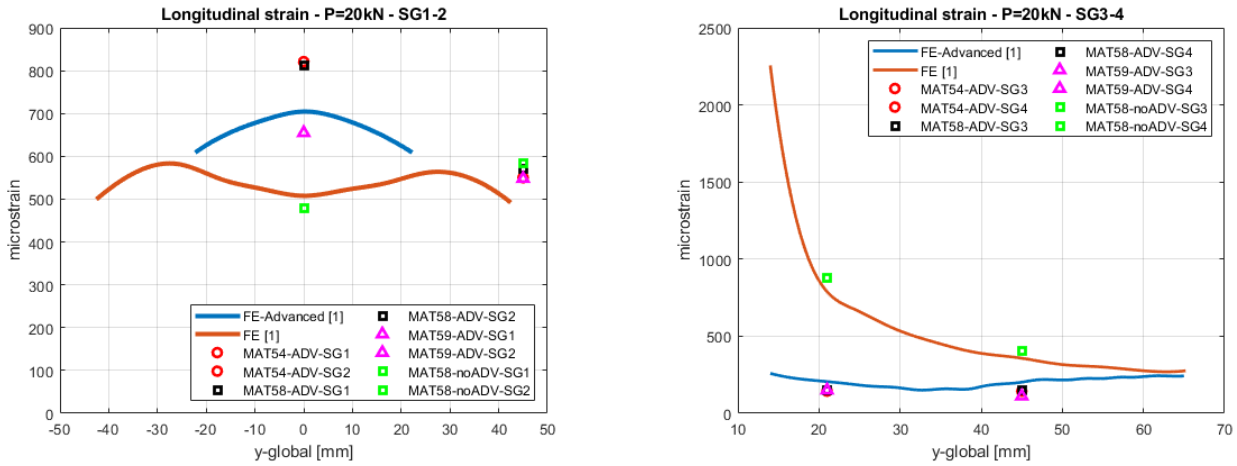

Figure 14: Strain comparison for SG 1-2-3-4 between static FE [1] and LS-DYNA simulations.

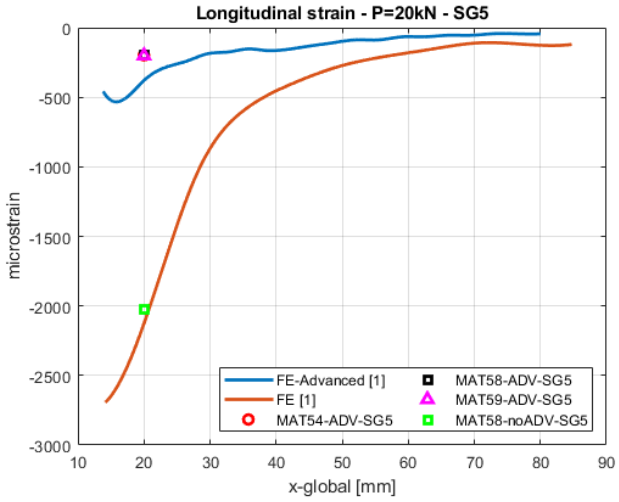

Figure 15: Strain comparison for SG 5 between static FE [1] and LS-DYNA simulations.

6. Conclusion

A complete high-fidelity shell-cohesive numerical procedure has been detailed to establish the mechanical response (elastic, plastic & failure) of the composite joint configuration proposed by Frulla & Romeo [1] under static load. The simulation results, in agreement with experimental observations, demonstrate that the proposed numerical technique is capable of predicting the initiation ad propagation of damage that led to the failure of the composite joint. In particular, the proposed numerical model is capable to evaluate and define the non-linear behaviour observed by composite joints when loaded in control displacement and to reproduce the strain-field reconstructed experimentally. Principal material and numerical parameters have been proposed for different material formulations available in LS-DYNA R11.1. Several comparisons of different material models have been evaluated in this study. Best numerical results obtained from the described numerical campaign are reported and compared with the experimental results. The results obtained show that the application of MAT54 and MAT58 with both elastic and crushable foam formulation set the best results for static failure and fracture analysis as refereed to experimental simple case. MAT58 with MAT63 crushable foam exhibit the best results in comparison to experimental static tests. Calibrated numerical models demonstrate a relative sensitivity the damage process adopted for the calibration of the erosion parameters. A structured evaluation is required to select the appropriate numerical erosion parameter. Preliminary test-analysis correlation indicates that the selected modeling technique adopted for this study could be used to predicts experimental results with a reduced computational cost when compared to the proposed laboratory tests of the flat composite sandwich joint.

Copyright Statement

References

[1] Frulla. G, Romeo G. Numerical/experimental structural characterization of composite advanced joints for HALE-UAV platforms, Composites Part B: engineering; 39 (2008) 656-664.

[2] Romeo G, Frulla G. Bearing Strength of Bolted Joints in CFRP Wing Fittings, 23rd ICAS Congress 8-13 September 2002 – Toronto, Canada.

[3] Romeo G, Frulla G. Experimental behaviour of composite advanced joint under cyclic loads. ICAF Congress 6-10 June 2005 – Hamburg, Germany.

[4] Zhang K, Ueng CES. Stresses around a pin-loaded hole in orthotropic plates, J Compos Mater 1984;18(5):432–46, September.

[5] Romeo G, Frulla G. Experimental behavior of composite advanced joint under cyclic loads, ICAF05-International Committee on aeronautical fatigue. Hamburg, Germany: 6–10 June 2005. Paper 064. p. 11.

[6] Anon. Engineered materials handbook – composites, vol. 1. ASM International; 1987.

[7] Wang HS, Hung CL, Chang FK. Bearing failure of bolted composite joints, J Compos Mater 1996;30(12):1285–313.

[8] Wright RJ, Johnson WS, Sacks S, Ahmed H. Bolt bearing behaviour of highly loaded polymer matrix composite joints at elevated temperatures, with and without clamp-up, J Compos Tech Res, JCTRER 2000 2000;22(1):33–9.

[9] Haufe A, Cavariani S, Liebold Chr, Usta T, Kotzakolios Th, Giannaros E, Kostopoulos V, Hornig A, Gude M, Djordjevic N, Vignjevic R, Meo M. On Composite Model Calibration for Extreme Impact Loading Exemplified on Aerospace Structures. 16th International LS-DYNA® Users Conference, Detroit, 2020

[10] Hunziker KJ, Pang JK, Melis ME, Pereira JM, Rassaian M. NASA ACC High Energy Dynamic Impact Methodology and Outcomes. AIAA Conference, 2018

[11] Justusson B, Pang J, Molitor M, Rassaian M, Rosmann R. An Overview of the NASA Advanced Composites Consortium High Energy Dynamic Impact Phase II Technical Path. AIAA Conference, 2019

[12] Cestino E, Romeo G, Piana P, Danzi F. Numerical/experimental evaluation of buckling behaviour and residual tensile strength of composite aerospace structures after low velocity impact, Aerospace Science and Technology; vol 54 (2016) 1-9

[13] Polla A, Piana P, Cestino E, Frulla G. Delamination and fracture modeling techniques for shell composite structures in LS-DYNA®, 13th European LS-DYNA Conference 4-7 October 2021 – Ulm, Germany.

[14] Boria, S. 13 - Lightweight design and crash analysis of composites, Lightweight Composite Structures in Transport, 2016, Woodhead Publishing - Elsevier Ltd., 329-360.

[15] Hinton MJ, Soden PD. Predicting failure in composite laminates: the background to the exercise. Composites Science and Technology 1998, 58(7): 1001-1010.

[16] Soden PD, Hinton MJ, Kaddour AS. A comparison of the predictive capabilities of current failure theories for composite laminates. Composites Science and Technology 1998, 58(7): 1225-1254.

[17] LLorca J, González C, Molina-Aldareguía JM, Segurado J, Seltzer R, Sket F, Rodríguez M, Sádaba S, Muñoz R, Canal LP. Multiscale Modeling of Composite Materials: a Roadmap Towards Virtual Testing, Advanced Materials; Whiley-VCH (2011)

[18] Kona A, Bhasin A, Gomez L, Olivares G, Gomez A, Keshavanarayana S, Pang J, Molitor M, Rassaian M. Evaluation of LS-DYNA MAT162 for Modeling Composite Fastner Joints for High Rates of Loading, AIAA Scitech 2019 Forum 7-11 January 2019 – San Diego, California.

[19] Girolamo D, Dávila Carlos G, Leone Frank A, Lin S. Cohesive Laws and Progressive Damage Analysis of Composite Bonded Joints, a Combined Numerical/Experimental Approach. AIAA Conference, 2019

[20] "Keyword user's manual volume II: Material Models LS-DYNA R11", LIVERMORE SOFTWARE TECHNOLOGY CORPORATION (LSTC), 2018.

[21] Matzenmiller A, Lubliner J, Taylor RL. A constitutive model for anisotropic damage in fiber-composites, Mechanics of Materials 20 (1995) 125-152

[22] Turon A, Dàvila CG, Camanho PP, Costa J. An engineering solution for mesh size effects in the simulation of delamination using cohesive zone models, Engineering Fracture Mechanics, 2007, 74: 1665–1682.

[23] Abdel-Monsef S, Renart J, Carreras L, Maimí P, Turon A. Environmental effects on the cohesive laws of the composite bonded joints, Composites Part A 155 (2022) 106798